

A Model-Independent Framework for Gravitational-Wave Reconstruction of Binary Black Hole Hyperbolic Encounters in Ground-Based Interferometers

Peter Lott,^{1,2} Heleen Amedi,¹ Jay Graves,³ Yeong-Bok Bae,⁴ Margaret Millhouse,¹ and Laura Cadonati¹

¹*School of Physics, Georgia Institute of Technology, Atlanta, Georgia 30332, USA*

²*Phenikaa Institute for Advanced Study, Phenikaa University, Duong Noi, 12116 Hanoi, Vietnam*

³*Department of Physics, Yale University, New Haven, CT 06511, USA*

⁴*Department of Physics, Chung-Ang University, Seoul 06974, Republic of Korea*

(Dated: December 2, 2025)

Binary black hole hyperbolic encounters represent a dynamical interaction in which two black holes undergo a close fly-by, emitting gravitational-wave bremsstrahlung in the form of a short-duration, single-cycle transient. These events are expected to occur in dense stellar environments such as globular clusters and both active and quiescent galactic nuclei. In this work, we constrain the detection sensitivity for hyperbolic encounters of black hole pairs with a range of asymmetric masses. We employ BayesWave, a wavelet-based morphology-independent algorithm to characterize hyperbolic encounter waveforms in simulated detector noise; for this study, we explore the use of exponential shapelets. We find that a typical hyperbolic orbit with total mass $20 M_{\odot}$ can be detected up to distance $d_L \sim 40 - 200$ Mpc, and we forecast the possibility of detection by ground-based current and future gravitational wave interferometers.

I. INTRODUCTION

The Laser Interferometer Gravitational-Wave Observatory (LIGO), Virgo and KAGRA detectors (LVK) have to date published more than 200 gravitational wave (GW) events from mergers of compact objects in bound orbits [1, 2]. Most of these events are Binary Black Hole (BBH) coalescences, although systems with neutron stars have also been detected [3–6]. The increasing sensitivity of current ground-based detectors, as well as prospects for next-generation interferometers such as Cosmic Explorer (CE) [7] and Einstein Telescope (ET) [8], have widened the potential discovery window. For example, recent work proposed BBH hyperbolic encounters as a viable source of GW radiation detectable in ground-based interferometers [9–12]. In two-body fly-by interactions, GWs are emitted as *GW bremsstrahlung*; for binary masses in the LIGO band [13] if the encounters are sufficiently close, this radiation can reach the sensitivity band of ground-based interferometers like LIGO and Virgo. As a GW source, BBH hyperbolic encounters are a unique probe for black holes, as their extreme eccentricity can constrain formation channels, in conjunction with radiation-driven dynamical captures [14]. BBH hyperbolic encounters may also make up a non-negligible portion of the stochastic GW background, particularly in the primordial black hole hypothesis [15–17].

Physically, the hyperbolic encounter can be described as a classical two-body problem in an unbound orbit, characterized by the eccentricity $e \gtrsim 1$, the initial relative velocity v_0 , the total mass M and the impact parameter b , a length-scale property of the orbit. As the system evolves, the trajectory of the secondary black hole is perturbed by the gravitational field of the primary black hole, resulting in a *braking radiation* analogous to electromagnetic bremsstrahlung. Thus, the problem can be described with a relatively small number of

parameters whose waveforms may be approximated by similar methods as in the merger case [13]. For this reason, the hyperbolic two-body problem has seen treatment in post-Newtonian [18–21] and post-Minkowskian [22–26] approximations. Numerical relativity simulations of BBH hyperbolic encounters in unequal masses [27–29] have revealed a morphology rich in spin effects [28], including ringdown effects [29].

From a data analysis standpoint, BBH hyperbolic encounter GW signals are morphologically distinct from their merger counterparts: they are single-cycle, i.e., broadband, as opposed to quasiperiodic BBH merger waveforms. In addition, their waveforms exhibit the linear memory effect, which binary mergers typically do not due to their rotational symmetry, although there are exceptions [30, 31]. A search has been carried out for BBH hyperbolic encounters in data from the third LVC observing run (O3) [11, 12], but no significant events have been confirmed. The rate estimates show that they can reach a few per year [9, 13, 32] in the upgraded version of LIGO, A+ [33].

In this work, we present a study of simulated signals of GW radiation from black holes in unbound orbits. The motivation for this study is two-fold. For one, the inner dynamics of globular clusters and active galactic nuclei disk scenarios could be a perfect environment for fly-by orbits between compact objects, as has been demonstrated in several many-body simulations [34–36]. Detection of GW emission could provide insight into black hole populations in these environments [9]. For another, BBH hyperbolic encounters present a challenge in data analysis. Given that they are morphologically distinct from the chirp-like profile exhibited by circular binaries, BBH hyperbolic encounters may provide a unique opportunity to test the waveform systematics of model-dependent and independent algorithms alike.

In this paper, we employ waveforms from a numerical simulation of BBH hyperbolic encounters with un-

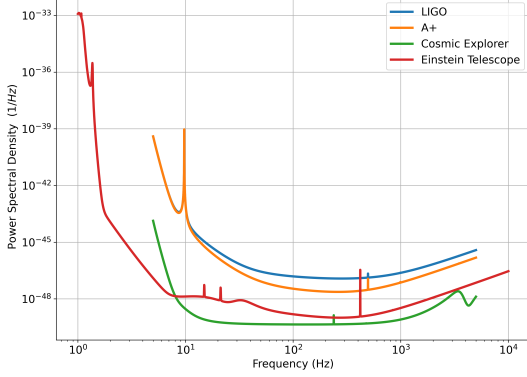


FIG. 1. Sensitivity curves for LIGO [37], A+ [33], Cosmic Explorer [7], and Einstein Telescope [8] (data from [38]). Previous estimates [12, 32] suggest that hyperbolic encounters are most common around 10 Hz. Detectors with improved low-frequency sensitivity, such as Cosmic Explorer and the Einstein Telescope, are better suited to capturing these signals than current-generation instruments like LIGO or even A+.

equal masses [27]. The waveforms are quadrupolar-mode and spinless, spanning a grid of waveform parameters. To reconstruct the waveform we use BayesWave [39, 40], a model-agnostic Bayesian inference algorithm that resolves features in the data without assuming a-priori knowledge of the signal. We use these simulated signals (hereafter referred to as *injections*) to empirically constrain detection rates for LIGO, A+ CE and ET [41]. The strain sensitivity for the four detectors is presented in Figure 1.

For this exploratory work, we employ *exponential shapelets* [42] as frame functions and compare their reconstruction faithfulness to frames previously used in morphology-independent analyses [12, 39, 43–45].

II. GW BURST RECONSTRUCTION

A. BayesWave

BayesWave is a model-agnostic algorithm for gravitational-wave inference that reconstructs transient features in detector data using a sum of frame functions [39, 40, 46]. Unlike templated analyses [47–49], BayesWave does not return posterior distributions of the physical parameters of the gravitational-wave signal; rather, it returns a posterior distribution of the signal $\mathbf{h}(t)$ itself, via the Bayes' Theorem:

$$p(\mathbf{h}|\mathbf{d}) = \frac{p(\mathbf{h})p(\mathbf{d}|\mathbf{h})}{p(\mathbf{d})}, \quad (1)$$

where \mathbf{d} is the detector data (which, in the absence of a signal, we assume to be stationary and Gaussian),

$p(\mathbf{h})$ is the prior knowledge about the system, $p(\mathbf{d}|\mathbf{h})$ is the likelihood, and $p(\mathbf{d})$ is the evidence. BayesWave draws from this posterior $p(\mathbf{h}|\mathbf{d})$ using a reversible-jump Markov chain Monte Carlo (RJMCMC), which samples over the frame function parameters as well as the number of frame functions. By using an RJMCMC that allows us to sample transdimensionally (i.e., adding or subtracting frame functions), BayesWave can faithfully reconstruct a wide range of signal morphologies, may fair better than template-based reconstructions in situations where information about the model is incomplete (e.g. higher order modes or physics beyond GR) [39, 40, 45, 46]. Due to its inherent flexibility, BayesWave has been used in the processing of events in GW transient catalogs [50–53], for tests of general relativity [54, 55], and in the mitigation of instrumental glitches [56–58].

Two frame function classes have been previously implemented in BayesWave: sine-gaussians (also called *Morlet-Gabor* wavelets), and *chirplets* [40, 46].

Morlet-Gabor wavelets are maximally compact in time-frequency, and have an analytic expression for the Fourier transformation, which is beneficial since BayesWave calculates the likelihood in the frequency domain [39]. Their time-domain expression is:

$$\Psi_{\text{Morlet-Gabor}}(t; t_0, f_0, Q, A, \phi_0) = A e^{-(t-t_0)^2/\tau^2} \cos(2\pi f_0(t-t_0) + \phi_0) \quad (2)$$

where t_0 and f_0 are the central time and the central frequency, ϕ_0 is the phase offset, A is the amplitude, and $Q = \Delta t \Delta f$, is the *quality factor*. We also define $\tau = Q/2\pi f_0$ for convenience. Their Fourier transform is:

$$\Psi_{\text{Morlet-Gabor}}(f; t_0, f_0, Q, A, \phi_0) = \frac{\sqrt{\pi} A \tau}{2} e^{-\pi^2 \tau^2 (f-f_0)^2} e^{-2\pi i f t_0} (e^{i\phi_0} + e^{-i\phi_0} e^{-Q^2 f/f_0}). \quad (3)$$

Chirplets mathematically differ from Morlet-Gabor wavelets in the time domain by a frequency evolution term which allows for the chirplet's frequency to smoothly increase or decrease over time [46, 59]:

$$\Psi_{\text{chirplet}}(t; t_0, f_0, Q, A, \phi_0, \dot{f}_0) = \frac{\sqrt{\pi} A \tau}{2} A e^{-(t-t_0)^2/\tau^2} \cos(2\pi f_0(t-t_0) + \pi \dot{f}_0(t-t_0)^2 \phi_0), \quad (4)$$

where $\tau = Q/2\pi f_0$. The parameter \dot{f}_0 , can be positive or negative and describes the linear increase or decrease of frequency over time. The analytical expression for chirplets in the frequency domain can be found in [46].

Morlet-Gabor wavelets and chirplets have both been shown to accurately reconstruct simulated GW signals [45, 60–62]. For compact binary coalescences, which increase in frequency up to the merger, the added flexibility of the \dot{f}_0 parameter in chirplets leads to larger overlaps between the injected signal and the waveform

recovered by BayesWave. However, for white noise burst test signals, with no well defined frequency evolution, chirplets and wavelets have been shown to perform comparably [46]. Outside of BayesWave, Morlet-Gabor and chirplet bases have proven beneficial in time-frequency GW Compact Binary Coalescence (CBC) analysis, particularly with modulation Q to extract the postmerger component of a NS-NS binary [63].

B. Shapelets

In this work, we investigate *shapelets* [42, 64] as a new set of BayesWave frame functions, following their prior use in searches for gravitational lensing [65–67], exoplanets [68, 69], pulsar timing [70, 71], and other astrophysical phenomena [72]. Shapelets are Hermite functions multiplied by an envelope function. We employ the *exponential shapelets* variant [42, 64] recently used in a LISA Pathfinder glitch analysis [64]. Using an exponential envelope introduces heavier tails and asymmetry, making exponential shapelets better suited for capturing sharp or extended GW features [42], compared to the more localized Gaussian shapelets [39, 44, 46].

Shapelets are a complete and orthogonal set [42, 65]. Their time-domain expression is:

$$\Psi_{shape}(t; t_0, f_0, Q, A) = \frac{(-1)^{n-1}A}{\sqrt{n^3\beta}} \left(\frac{2(t-t_0)}{n\beta} \right) L_{n-1}^1 \frac{2(t-t_0)}{n\beta} e^{-(t-t_0)/n\beta} e^{-2\pi i t f_0}, \quad (5)$$

where $\beta = Q/2\pi f_0$, $L_{n-1}^1(t-t_0)$ is the first-order generalized Laguerre polynomial. In the frequency domain, they can be expressed as:

$$\tilde{\Psi}_{shape}(f; t_0, f_0, Q, A) = (-1)^n A \sqrt{\frac{2n\beta}{\pi}} \frac{(n\beta(f-f_0) - i)^{2n}}{((n\beta(f-f_0)^2 + 1))^{n+1}} e^{-2\pi i t_0 f}. \quad (6)$$

Though Eq. 5 is only valid for $t > t_0$, because the analysis is performed in the frequency domain and only inverse Fourier transformed into the time domain for visualization purposes; in practice $\Psi_{shapelet}(t) = 0$ for $t < t_0$.

For reference, $n = 0$ to $n = 3$ shapelets $\tilde{\Psi}_n$ are plotted in the Fourier and time domains in Figure 2. As the index number n increases, the Laguerre term in $\tilde{\Psi}_n$ dominates and the number of oscillations increases as a function of frequency. For simplicity, this study is restricted to shapelets with $n = 2$.

The primary motivation for using shapelets is their morphological resemblance to gravitational-wave signals from hyperbolic encounters. Transdimensional MCMCs balance the complexity of a model (i.e. the number of frame functions used to reconstruct a signal) against how well it fits the data. Chirplets were motivated by compact binary coalescences, the most abundant GW source,

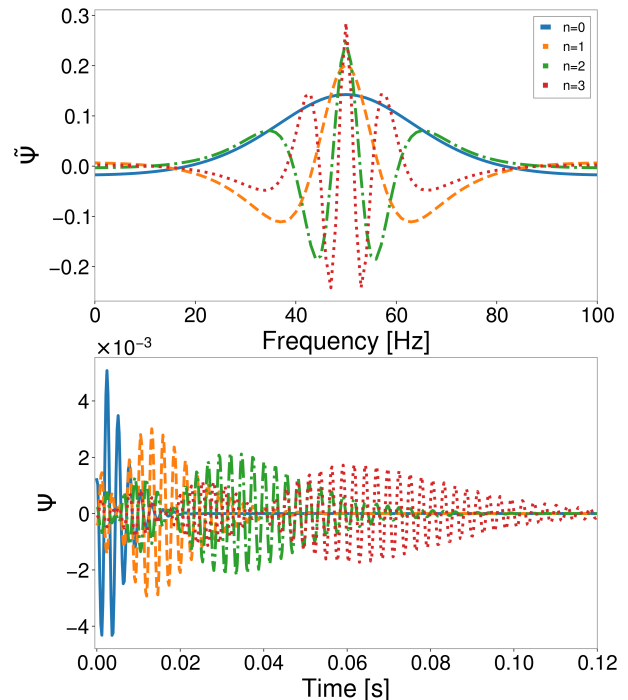


FIG. 2. Examples of $n = 0, 1, 2, 3$ shapelets in the frequency domain (top), and time domain (bottom). For all shapelets, $Q = 20$, $f_0 = 200\text{Hz}$, and $t_0 = 0\text{s}$.

which exhibit continuously increasing frequency, and indeed they improved BayesWave reconstructions of binary black hole simulations [46]. Given the resemblance between shapelets and hyperbolic encounter waveforms, we test whether shapelets outperform wavelets and chirplets at reconstructing simulated hyperbolic signals.

The implementation of shapelets in BayesWave is nearly identical to that of chirplets and Morlet-Gabor wavelets, sampling parameters t_0, f_0, Q and A but without a phase parameter ϕ_0 . We use the same priors as [40]: flat priors for t_0, f_0, Q , while the prior on A is actually a prior on the frame function’s signal-to-noise ratio (SNR). The SNR of frame function ψ is $\text{SNR} = \sqrt{(\psi|\psi)}$, where the round brackets denote the noise-weighted inner product:

$$(a|b) = 2 \int_0^\infty \frac{\tilde{a}^* \tilde{b} + \tilde{a} \tilde{b}^*}{S_n(f)} df, \quad (7)$$

where $S_n(f)$ is the one-sided noise power spectral density. For shapelets, we use the approximation:

$$\text{SNR}^2 \approx \frac{4A^2}{S_n(f_0)}. \quad (8)$$

For all wavelet models, the prior on the number of wavelets D is empirically derived from BayesWave’s unmodeled search of data from LIGO’s first observing run:

$$p(D) = \frac{4\sqrt{3}D}{2\pi a^2(3 + \frac{D}{a})^4}, \quad (9)$$

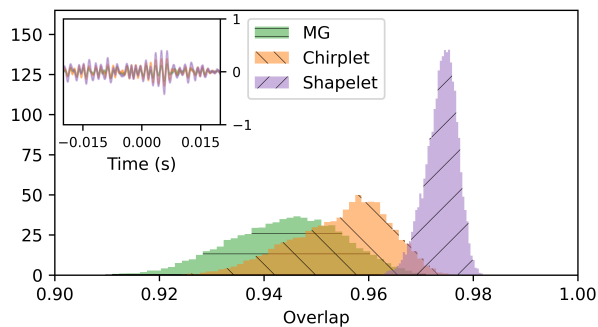


FIG. 3. Example BayesWave waveform reconstruction of simulated white noise bursts (WNBs) with the three frame function families used in this study. WNBs are unpolarized signals with complicated frequency structure, (due to their localization in time) providing a good test for the faithfulness of BayesWave’s reconstruction.

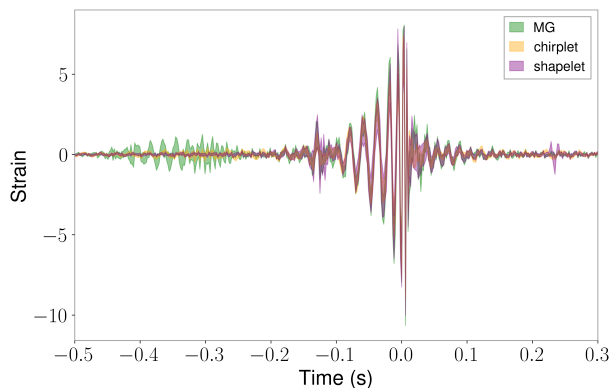


FIG. 4. Time-domain reconstruction of GW150914, the first GW event, using BayesWave with shapelets and the standard Morlet-Gabor wavelet reconstructions, respectively. This analysis corresponds to LIGO-Hanford.

with $a = 2.9$ [40].

C. Comparing frame functions

We compare the performance of shapelets with other BayesWave frame functions using simulated signals and gravitational wave data.

For simulated signals, we quantify the BayesWave reconstruction accuracy as the *overlap* between injected (h_{inj}) and reconstructed (h_{rec}) waveforms:

$$\mathcal{O} \equiv \frac{(h_{inj}|h_{rec})}{\sqrt{(h_{inj}|h_{inj})(h_{rec}|h_{rec})}}. \quad (10)$$

As a test case, we reconstruct *white noise bursts*, instances of excess Gaussian strain with limited duration and bandwidth. Fig. 3 shows overlap histograms for reconstructing one such simulation, with 150 Hz central frequency, 100 Hz bandwidth, 0.1 s duration, and SNR=30

in ideal LIGO noise (see Fig. 1) with optimal sky location. The overlaps are drawn from the BayesWave posterior distribution. We found similar trends for different parameter choices. As they are not tied to any astrophysical model, white noise bursts are well suited to test the robustness and flexibility of model-independent data analysis methods [73]. The overlap distribution for shapelets is centered around larger overlap values than the other two frame functions, suggesting better performance in capturing the structure of this particular simulated white noise burst signal.

Fig. 4 instead shows the reconstructed waveforms for GW150914, the first discovered BBH GW event detected with a network signal-to-noise ratio of 24 [74]. Reconstructions using Morlet-Gabor, chirplet, and shapelet frames yield similar results, with overlaps of 0.934, 0.935, and 0.928, respectively, when compared to the best-fit waveform from general-relativity based estimation. We note also that the Morlet-Gabor and shapelet reconstructions exhibit pre- and post-merger artifacts, which is a common feature in wavelet-based analyses [75, 76]. These artifacts arise from the overcomplete nature of the frames and the tendency of the model to fit excess power near the signal boundaries, often due to limited time-frequency localization or mismatch between the frame and localized signal features. It is important to note that the overlaps reported for GW150914 are maximum a posteriori 3 are derived from the full posterior distribution. The lower overlaps for GW150914 are expected, as it is a real astrophysical signal with complex morphology and sky projection effects, in contrast to the short, high-SNR, and morphologically simpler white-noise burst used in Fig. 3.

III. HYPERBOLIC ENCOUNTERS

A. Waveforms

We utilized numerical simulations from a study of the critical cross section for dynamical capture of two black holes [27]. The original study mapped energy and angular momentum of hyperbolic orbits over a wide parameter space and simulated parabolic orbits, assuming nearly identical gravitational wave emission due to similar orbital shapes at periapsis. While parabolic orbits represent the threshold between bound and unbound motion, hyperbolic and parabolic orbits are indistinguishable for burst GW detection purposes. For a fixed energy, varying the angular momentum is equivalent to considering different impact parameters. Based on angular momentum magnitude, orbits can be classified as either direct merging or fly-by. Here, we used the quadrupolar dominant ($l = 2, m = 2$) mode in spin-weighted spherical harmonics from the fly-by orbit, as shown in Fig. 5. The orbit characteristics vary with the mass ratio of the two black holes and the total angular momentum (see 6), which in turn affects the wavelength and intensity of the emitted

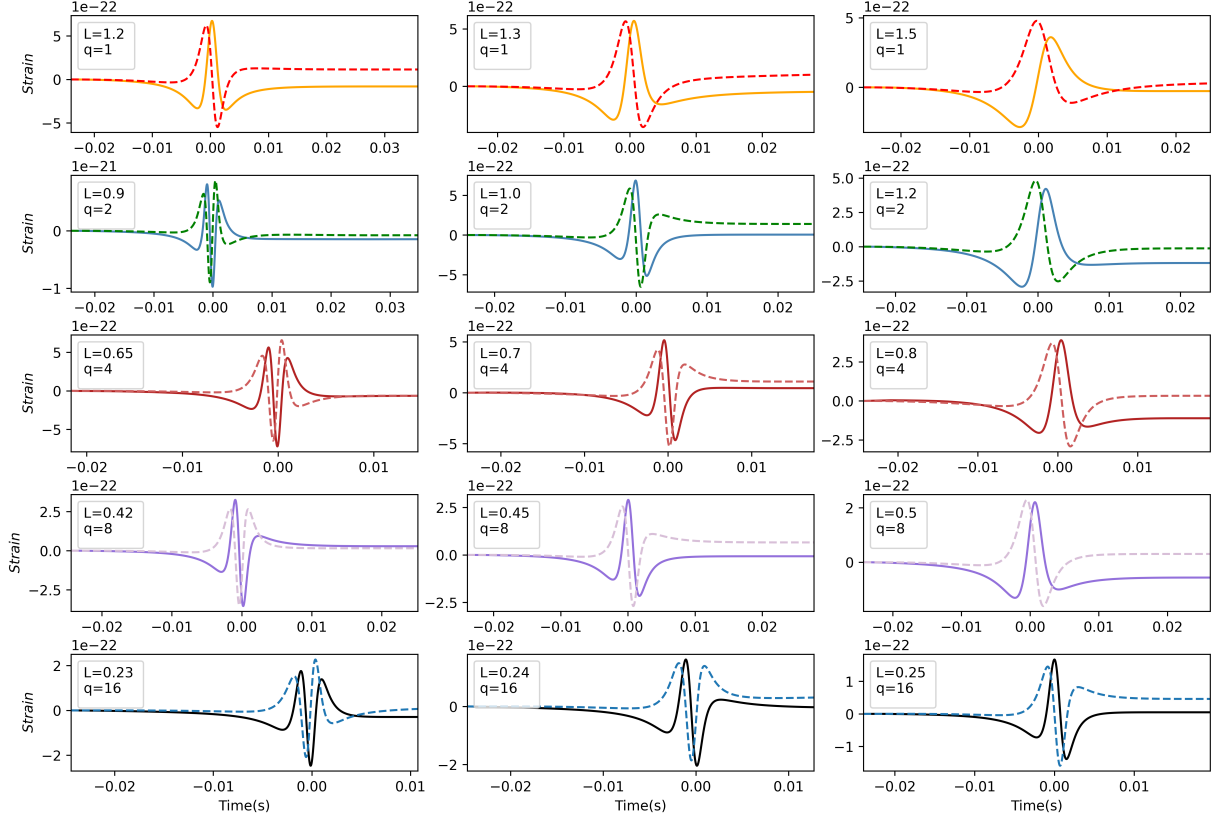


FIG. 5. Waveforms used for this analysis, from face-on binaries with total mass $20 M_{\odot}$. Each panel displays is a waveform with plus (solid) and cross (dashed) polarization. This grid spans a parameter space with mass ratios $q = [1, 2, 4, 8, 16]$ (displayed row-wise) and several initial angular momenta, represented column-wise. The waveforms are more narrowly spaced out in time for a larger mass ratio.

gravitational waves. Previous studies [32, 77] demonstrated that hyperbolic encounters of BBH systems are typically nearly parabolic, and signals from strictly hyperbolic orbits do not differ significantly from parabolic orbits when estimating detection rates. For simplicity, we considered only binaries with zero inclination (face-on orientation).

B. Analysis Setup

We injected numerical simulations from [27] representing GW emission from BBH hyperbolic encounters. Our dataset includes fifteen waveforms spanning mass ratios $q = [1, 2, 4, 8, 16]$. The initial angular momenta and, consequently, the impact parameters were selected to ensure that the encounters produce sufficient luminosity to be detectable while avoiding dynamical capture leading to coalescence. These waveforms were injected into simulated Gaussian noise colored to match the power spectral density $S_n(f)$ of an idealized two-detector network. We then used BayesWave to recover and analyze these signals. The initial parameters for this simulation study are listed in Table I.

For each injection, we calculated the signal-to-noise ratio (SNR) to determine the maximum detectable distance and the overlap distribution across iterations, which provides a quantitative measure of the reconstruction's faithfulness to the original signal.

We adopted uniform priors on the frame function parameters, within these bounds:

- time: $t_{min} \leq t_0 \leq t_{max}$, including a 1 s interval centered on the peak amplitude of the injection;
- frequency: $f_{min} \leq f_0 \leq f_{max}$ where f_{min} is set at 20 Hz and f_{max} is the Nyquist frequency (4096 Hz in our case, determined by the sampling rate);
- quality factor: $0.1 \leq Q \leq 40$;
- phase: $0 \leq \phi \leq 2\pi$.

We use the prior on the number of frame functions as described in Eq. 9. We conducted our analysis using BayesWave with 4-second segments and 4096 Hz sampling rate, reconstructing each waveform with the three frame functions (Morlet-Gabor, chirplet, and shapelet). This process was repeated for LIGO, A+, CE, and ET power spectral densities, totaling 180 injections.

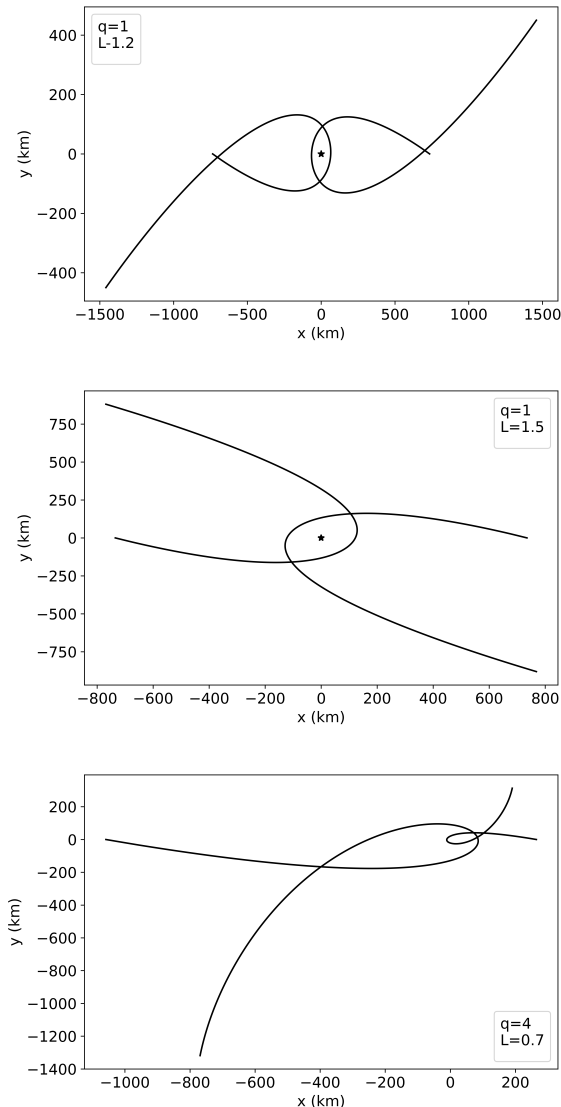


FIG. 6. Trajectories for three of the waveforms used in this study, with input parameters $(q, L) = (1, 1.2)$ (top), $(q, L) = (1, 1.5)$ (center), $(q, L) = (4, 0.7)$ (bottom)

For each frame function, we calculate the overlap \mathcal{O} between the reconstructed and injected signals, where $\mathcal{O} = 1$ indicates complete agreement. The noise curves used were extracted from the publicly available LIGO sensitivity design curves [41] and are shown in Fig. 1.

IV. RESULTS

We present our main results on the basis of the analytical framework described above. First, we evaluate BayesWave reconstruction faithfulness by examining overlap distributions for each frame function and analyzing which waveform characteristics favor shapelets over other methods. We then calculate detection rates for

LIGO, A +, CE, and ET, based on the event rate estimates of Kocsis et al. [32], identifying regions of the parameter space with the highest detection probability.

A. Comparison of frame functions

Figure 7 compares BayesWave reconstruction performance with the three frame functions across hyperbolic encounter parameters. Panels are arranged by mass ratio (top to bottom) and initial angular momentum (left to right), showing overlap posteriors and 90% credible waveform reconstructions.

Across the parameter space, all frame functions produce overlaps greater than 0.9, indicating they can all reconstruct the hyperbolic encounters well. We see nearly identical overlap distributions for chirplets and wavelets. This result is not unexpected, as chirplets reduce to wavelets when $\dot{f}_0 = 0$ (see Eq. 4). The distribution of overlaps using shapelets for the reconstruction are noticeably distinct from the chirplets and wavelets results; sometimes the shapelet-based reconstruction produces higher overlaps on average (for example $(q, L) = (2, 1.0)$), and sometimes lower overlaps on average (for example $(q, L) = (4, 0.65)$). This potentially points to limitations from restricting the shapelet index to $n = 2$, and future work can investigate changing that index.

In addition to reconstruction fidelity, we also investigate the typical model dimensionality for the three frame functions. Figure 8 shows the average (mean) number of frame functions used per BayesWave run for each hyperbolic waveform described in Sec. IIIB, injected with SNRs uniformly distributed from 10 to 40. While the number of shapelets used peaks at a lower value (close to one) compared to wavelets and chirplets, the tail of the shapelets distribution extends to higher values. This indicates that while chirplets and wavelets provide consistently high overlaps, shapelets sometimes achieve higher or lower overlaps depending on the waveform, and the broader tail of their distribution suggests that more components may occasionally be required, implying that shapelets could be chosen when capturing complex waveform features is a priority, while chirplets or wavelets may be preferred for efficiency in simpler cases.

We additionally compare the computational efficiencies of the different frame functions. Table II shows that shapelets use less disk space but require more memory and CPU time than Morlet-Gabor and chirplet frames.

B. Detection rates

In this study, we declare that a detection occurs when the recovered signal SNR exceeds 8, consistent with other similar work [37]. Since the SNR is proportional to the waveform amplitude h , (see Eq. 7), it is inversely proportional to the (horizon) luminosity distance d_L , the largest

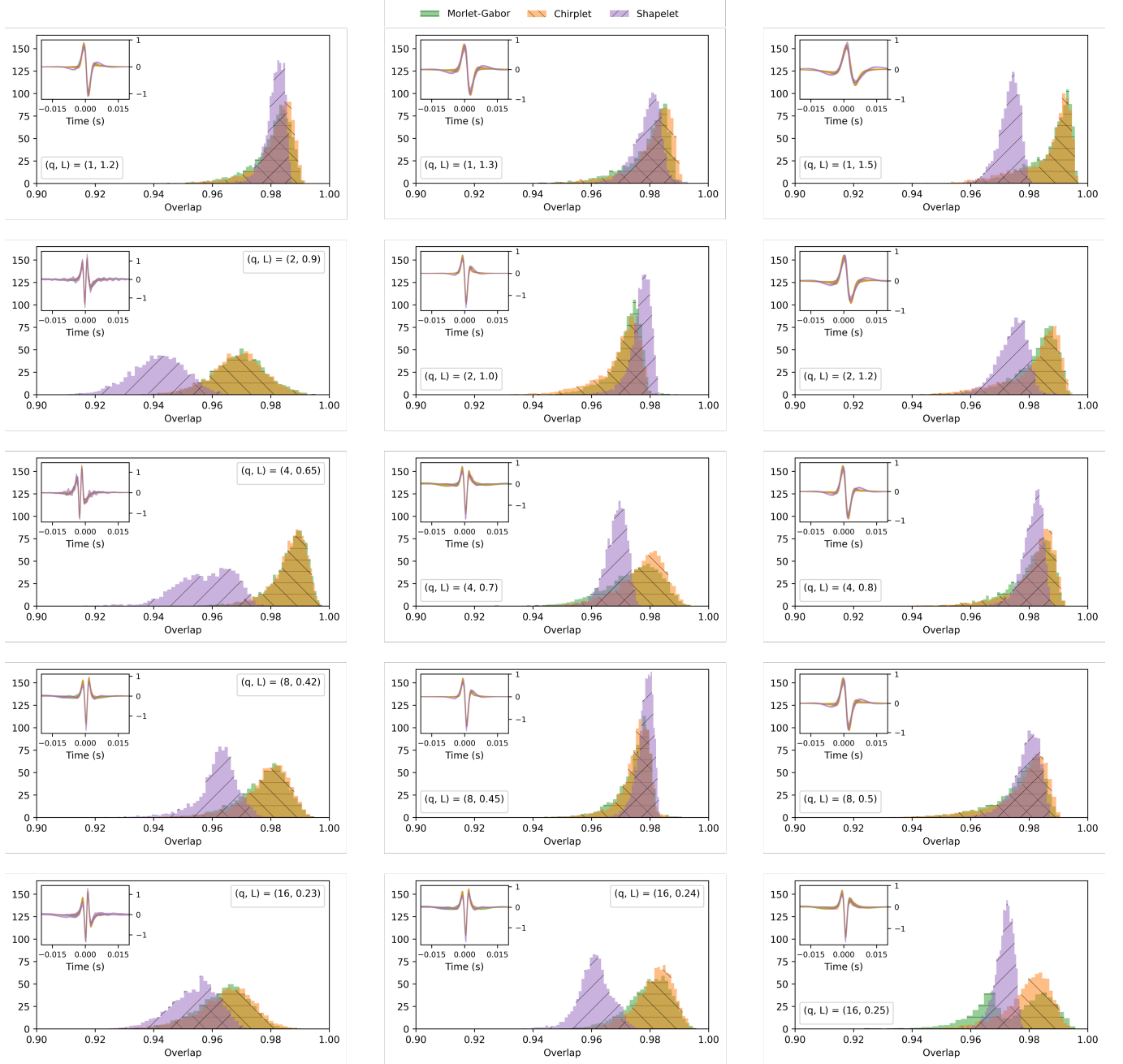


FIG. 7. Comparison of waveform reconstructions with three frame functions. In each panel, the inset plot is the 90 percent credible interval whitened waveform reconstruction using the Morlet-Gabor (green), chirplet (orange), and shapelet (purple), with time on the abscissa and dimensionless strain on the ordinate. The main plot in each panel is the posterior distribution of the overlaps between the injected waveform and the Morlet-Gabor, chirplet, and shapelet reconstructions (same colors as the inset plots). One can see that in nearly all cases, the overlaps distribution of chirplet and Morlet-Gabor is nearly identical, owing to their similar parameterizations.

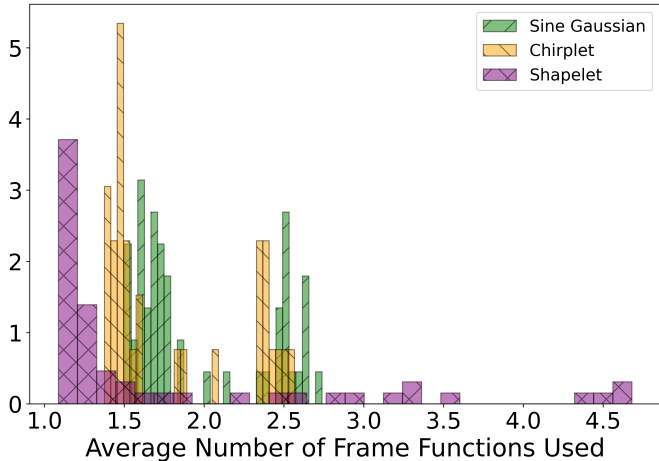


FIG. 8. Average number of frame functions used in three frame function types—Morlet-Gabor, Chirplet, and Shapelet—for the reconstructions of hyperbolic encounter waveforms using Morlet-Gabor wavelets, chirplets and shapelets. Note that the distributions for Morlet-Gabor and chirplet exhibit double peaks, indicating two parts of the reconstructed parameter space.

distance at which the signal is detectable:

$$\text{SNR} \sim \frac{1}{d_L} \quad (11)$$

For non-negligible redshift ($z \approx 0.05$) we must consider the rate of cosmological expansion, using the *redshifted sensitivity volume*:

$$V_z = 4\pi \int_0^{z_{\max}} (1+z) \frac{dV_C}{dz} dz, \quad (12)$$

where z_{\max} is defined as the maximum redshift at which a source would produce an SNR of exactly 8 in the detector, $\frac{dV_C}{dz}$ is the *differential comoving volume*:

$$\frac{dV_C}{dz} = 4\pi \frac{d_L^2}{E(z)(1+z)^2} \quad (13)$$

and $E(z) = \sqrt{\Omega_\Lambda + \Omega_m(1+z)^3}$. Ω_Λ and Ω_m are the fractions of mass-energy contained in vacuum energy, and matter, respectively.

The detection rate ν for a given waveform is related to the sensitivity volume by:

$$\nu = \mathcal{R}V, \quad (14)$$

with \mathcal{R} the expected rate for hyperbolic encounters in globular clusters. For all waveforms, we use the expected rate derived by Kocsis et al. [32].

Table I reports the calculated luminosity distance constraints and detection rates for BBH hyperbolic encounters, using the injection set from Section III, assuming

idealized noise and optimal sky orientation for a LIGO-type detector; our results are therefore optimistic. Actual noise (thermal, electronic, seismic) can distort the signals and reduce their detectability, while non-optimal detector orientation and systematic errors introduce additional limitations and biases that are not captured under ideal conditions. We repeated this analysis for A+, Cosmic Explorer, and Einstein Telescope noise realizations.

Our order of magnitude luminosity sensitivity distances are comparable to previous calculations [9, 12, 32], with LIGO sensitivity distance ranging from 60 to 250 Mpc, consistent with previous studies [9, 12, 32]; Fig. 9 shows sensitivity distance contours as a function of the initial angular momentum (i.e., impact parameter) and the mass ratio.

The calculated rates suggest that these events are most likely detectable by the next generation of gravitational wave detectors, Cosmic Explorer and Einstein Telescope, with 2.66 events per year for equal mass cases with Cosmic Explorer. Next-generation detector rates are overall consistent with other studies [9].

V. CONCLUSION

Highly eccentric black hole binary systems are predicted to be common in globular clusters and dense astrophysical environments [9–11, 13, 32, 35]. In particular, BBH hyperbolic encounters of stellar-mass black holes should emit GWs manifesting as single-cycle transients in current ground-based detector frequency ranges [13, 32].

This paper presents a Bayesian analysis of numerical waveforms from BBH hyperbolic encounters and estimates detection rates for current and future ground-based interferometers. Our rates are consistent with previous work [9, 12, 32], $\sim 10^{-3}$ per year for LIGO and A+ and \sim few per year for Cosmic Explorer and Einstein Telescope.

The analysis was performed with BayesWave. We tested shapelet frame functions against traditional Morlet-Gabor and chirplet functions, using the overlap between injected h_{inj} and recovered h_{rec} waveforms. We found that BayesWave with shapelets provides comparable reconstruction quality while typically requiring fewer basis functions, possibly due to morphological similarity between shapelets and BBH hyperbolic encounters in the time-frequency domain. The computational requirements are tabulated in Table II.

Applying this analysis to real data will require addressing instrumental glitches, particularly blip glitches that morphologically resemble hyperbolic encounter waveforms and could cause false detections. BayesWave's Bayesian framework for distinguishing astrophysical signals from glitches may directly apply to hyperbolic encounters.

Given globular cluster models [32] and the expected increasing detector sensitivity, GWs from hyperbolic encounters are likely to be detectable in the future. Since

TABLE I. Tabulated results from numerical injections. The first and second columns are the mass ratio and the initial angular momentum in geometric units, respectively, i.e. the initial parameters of the BBH system corresponding to each injected waveform. The third through tenth columns are the sensitive luminosity distance and detection rate for LIGO, A+, CE, and ET, respectively.

| q | L | LIGO | | LIGO A+ | | Cosmic Explorer | | Einstein Telescope | |
|----|------|---------|-----------------------------|---------|-----------------------------|-----------------|--------------------------|--------------------|--------------------------|
| | | D [Mpc] | Rate [$10^{-3}/\text{y}$] | [Mpc] | Rate [$10^{-3}/\text{y}$] | [Mpc] | Rate [y^{-1}] | [Mpc] | Rate [y^{-1}] |
| 1 | 1.2 | 165 | 1.24 | 305 | 7.47 | 2676 | 2.66 | 1715 | 0.86 |
| | 1.3 | 141 | 0.800 | 256 | 4.47 | 2623 | 2.52 | 1470 | 0.58 |
| | 1.5 | 99 | 0.277 | 181 | 1.64 | 2116 | 1.48 | 1050 | 0.24 |
| 2 | 0.9 | 197 | 2.09 | 372 | 13.3 | 3081 | 3.75 | 1969 | 1.23 |
| | 1.0 | 164 | 1.22 | 304 | 7.33 | 2634 | 2.55 | 1720 | 0.87 |
| | 1.2 | 115 | 0.441 | 214 | 2.64 | 2272 | 1.77 | 1177 | 0.32 |
| 4 | 0.65 | 144 | 0.851 | 291 | 6.64 | 2237 | 1.70 | 1458 | 0.57 |
| | 0.7 | 124 | 0.537 | 231 | 3.30 | 2040 | 1.35 | 1257 | 0.38 |
| | 0.8 | 97 | 0.260 | 184 | 1.70 | 1723 | 0.87 | 989 | 0.20 |
| 8 | 0.42 | 80 | 0.147 | 153 | 0.991 | 1260 | 0.39 | 828 | 0.12 |
| | 0.45 | 71 | 0.103 | 132 | 0.646 | 1169 | 0.32 | 746 | 0.09 |
| | 0.5 | 58 | 0.056 | 110 | 0.380 | 1024 | 0.22 | 597 | 0.05 |
| 16 | 0.23 | 49 | 0.032 | 94.1 | 0.237 | 762 | 0.098 | 497 | 0.03 |
| | 0.24 | 45 | 0.027 | 87 | 0.188 | 728 | 0.087 | 442 | 0.02 |
| | 0.25 | 41 | 0.021 | 78 | 0.137 | 687 | 0.074 | 429 | 0.02 |

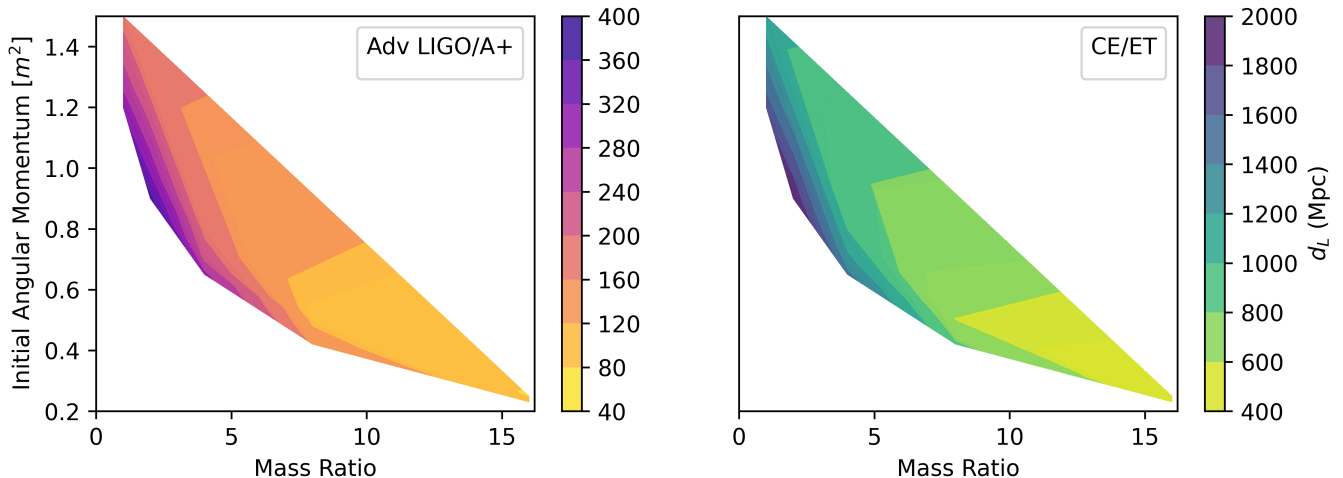


FIG. 9. Sensitivity distance contours from our waveform injections. For both panels, the ordinate is the initial angular momentum in geometric units of m^2 , and the abscissa is the mass ratio. The color bar shown to the right of each panel shows the luminosity distances at which the injection is detectable for SNR threshold 8, given an idealized noise spectrum. The left panel is for LIGO and A+ and the right panel is for CE and ET. Although our parameter space is limited, it is clear that the equal-mass ratio provides detectability at greater luminosity distance compared to the more extreme mass ratio counterparts, which is sensible because the gravitational radiation from bremsstrahlung encounters is proportional to the mass. The sensitivity range of 40 – 400 Mpc is consistent with estimates by [32], who examined an equal mass $m_1 = m_2 = 40 M_\odot$ case and found an estimated range of 200 Mpc for a threshold of SNR 5 studied the LIGO and A+ detector cases. Similarly, [12] found luminosity distances 40 – 50 Mpc range. The estimates presented here are comparatively optimistic, owing to the choice of idealized noise (i.e. no glitches).

dynamical evolution scenarios predict eccentric binary signatures [8], confirmed detections of hyperbolic encounters may inform black hole formation scenarios.

VI. ACKNOWLEDGMENT

This material is based upon work supported by NSF's LIGO Laboratory which is a major facility fully funded by the National Science Foundation. This research utilized data, software, and tools provided by the Gravitational Wave Open Science Center (<https://www.gw->

TABLE II. Approximate average disk memory usage and CPU time in reconstruction analysis.

| Frame Function | Disk Usage (MB) | Memory Usage (MB) | CPU Time (s) |
|----------------|-----------------|-------------------|--------------|
| Morlet-Gabor | 11.179 | 128 | 6172 |
| Chirplet | 14.474 | 129 | 6175 |
| Shapelet | 9.16 | 150 | 10991 |

openscience.org), a resource maintained by LIGO Laboratory, the LIGO Scientific Collaboration, and the Virgo Collaboration. LIGO's operations are funded by the U.S. National Science Foundation, while Virgo receives support from the French Centre National de Recherche Scientifique (CNRS), the Italian Istituto Nazionale di Fisica Nucleare (INFN), and the Dutch Nikhef, with additional contributions from Polish and Hungarian institutions. The authors also acknowledge the computational resources provided by the LIGO Laboratory, supported

by NSF Grants PHY-0757058 and PHY-0823459. This work was carried out using services offered by the OSG Consortium [59–62], funded by NSF awards 2030508 and 1836650. The GT authors express their gratitude to the NSF for funding under Grants PHY-1809572 and PHY-2110481. Y.-B.B. was supported in part by the National Research Foundation of Korea (NRF) grants funded by the Korea government (MSIT) (RS-2025-00556091 and RS-2025-00564350). The authors acknowledge John Wise, Daniel Williams, and Zoltan Haiman for illuminating discussions.

-
- [1] R. Abbott et al. GWTC-3: Compact Binary Coalescences Observed by LIGO and Virgo During the Second Part of the Third Observing Run, 11 2021. Preprint arXiv:2111.03606.
 - [2] A. G. Abac et al. GWTC-4.0: Updating the Gravitational-Wave Transient Catalog with Observations from the First Part of the Fourth LIGO-Virgo-KAGRA Observing Run. 8 2025.
 - [3] R. Abbott et al. Observation of Gravitational Waves from Two Neutron Star–Black Hole Coalescences. *Astrophys. J. Lett.*, 915(1):L5, 2021. doi:10.3847/2041-8213/ac082e.
 - [4] B. P. Abbott et al. GW170817: Observation of Gravitational Waves from a Binary Neutron Star Inspiral. *Phys. Rev. Lett.*, 119(16):161101, 2017. doi:10.1103/PhysRevLett.119.161101.
 - [5] B. P. Abbott et al. GW190425: Observation of a Compact Binary Coalescence with Total Mass $\sim 3.4M_{\odot}$. *Astrophys. J. Lett.*, 892(1):L3, 2020. doi:10.3847/2041-8213/ab75f5.
 - [6] R. Abbott et al. GW190814: Gravitational Waves from the Coalescence of a 23 Solar Mass Black Hole with a 2.6 Solar Mass Compact Object. *Astrophys. J. Lett.*, 896(2): L44, 2020. doi:10.3847/2041-8213/ab960f.
 - [7] D. Reitze et al. Cosmic Explorer: The U.S. Contribution to Gravitational-Wave Astronomy beyond LIGO. *Bull. Am. Astron. Soc.*, 51(7):035, 2019.
 - [8] M. Maggiore et al. Science Case for the Einstein Telescope. *JCAP*, 03:050, 2020. doi:10.1088/1475-7516/2020/03/050.
 - [9] Sajal Mukherjee, Sanjit Mitra, and Sourav Chatterjee. Gravitational wave observatories may be able to detect hyperbolic encounters of black holes. *Monthly Notices of the Royal Astronomical Society*, 508(4):5064–5073, 09 2021. ISSN 0035-8711. doi:10.1093/mnras/stab2721. URL <https://doi.org/10.1093/mnras/stab2721>.
 - [10] Marienza Caldarola, Sachiko Kuroyanagi, Savvas Nesseris, and Juan Garcia-Bellido. Effects of orbital precession on hyperbolic encounters. *Phys. Rev. D*, 109(6): 064001, 2024. doi:10.1103/PhysRevD.109.064001.
 - [11] Gonzalo Morrás, Juan García-Bellido, and Savvas Nesseris. Search for black hole hyperbolic encounters with gravitational wave detectors. *Phys. Dark Univ.*, 35: 100932, 2022. doi:10.1016/j.dark.2021.100932.
 - [12] Sophie Bini, Shubhanshu Tiwari, Yumeng Xu, Leigh Smith, Michael Ebersold, Giacomo Principe, Maria Haney, Philippe Jetzer, and Giovanni A. Prodi. Search for hyperbolic encounters of compact objects in the third LIGO-Virgo-KAGRA observing run, 2023. Preprint arXiv:2311.06630.
 - [13] Salvatore Capozziello and Mariafelicia De Laurentis. Gravitational waves from stellar encounters. *Astropart. Phys.*, 30:105–112, 2008. doi:10.1016/j.astropartphys.2008.07.005.
 - [14] Michael Ebersold, Shubhanshu Tiwari, Leigh Smith, Yeong-Bok Bae, Gungwong Kang, Daniel Williams, Achamveedu Gopakumar, Ik Siong Heng, and Maria Haney. Observational limits on the rate of radiation-driven binary black hole capture events. *Phys. Rev. D*, 106(10):104014, 2022. doi:10.1103/PhysRevD.106.104014.
 - [15] Juan García-Bellido, Santiago Jaraba, and Sachiko Kuroyanagi. The stochastic gravitational wave background from close hyperbolic encounters of primordial black holes in dense clusters. *Phys. Dark Univ.*, 36: 101009, 2022. doi:10.1016/j.dark.2022.101009.
 - [16] Juan Garcia-Bellido and Savvas Nesseris. Gravitational wave bursts from Primordial Black Hole hyperbolic encounters. *Phys. Dark Univ.*, 18:123–126, 2017. doi:10.1016/j.dark.2017.10.002.
 - [17] Juan García-Bellido and Savvas Nesseris. Gravitational wave energy emission and detection rates of Primordial Black Hole hyperbolic encounters. *Phys. Dark Univ.*, 21: 61–69, 2018. doi:10.1016/j.dark.2018.06.001.
 - [18] R O Hansen. Post-newtonian gravitational radiation from point masses in a hyperbolic kepler orbit*. *PHYSICAL REVIEW D VOLUME*, 5, 1972.
 - [19] M. Turner. Gravitational radiation from point-masses in unbound orbits: Newtonian results. *Astrophysical Jour-*

- nal, 216:610–619, September 1977. doi:10.1086/155501.
- [20] Gihyuk Cho, Achamveedu Gopakumar, Maria Haney, and Hyung Mok Lee. Gravitational waves from compact binaries in post-Newtonian accurate hyperbolic orbits. *Phys. Rev. D*, 98(2):024039, 2018. doi:10.1103/PhysRevD.98.024039.
- [21] Gihyuk Cho, Rafael A. Porto, and Zixin Yang. Gravitational radiation from inspiralling compact objects: Spin effects to the fourth post-Newtonian order. *Phys. Rev. D*, 106(10):L101501, 2022. doi:10.1103/PhysRevD.106.L101501.
- [22] K. S. Thorne and S. J. Kovacs. The generation of gravitational waves. I. Weak-field sources. *Astrophysical Journal*, 200:245–262, September 1975. doi:10.1086/153783.
- [23] R. J. Crowley and K. S. Thorne. The generation of gravitational waves. II. The postlinear formation revisited. *Astrophysical Journal*, 215:624–635, July 1977. doi:10.1086/155397.
- [24] S. J. Kovacs and K. S. Thorne. The generation of gravitational waves. III. Derivation of bremsstrahlung formulae. *Astrophysical Journal*, 217:252–280, October 1977. doi:10.1086/155576.
- [25] Jr. Kovacs, S. J. and K. S. Thorne. The generation of gravitational waves. IV. Bremsstrahlung. *Astrophysical Journal*, 224:62–85, August 1978. doi:10.1086/156350.
- [26] Justin Vines. Scattering of two spinning black holes in post-Minkowskian gravity, to all orders in spin, and effective-one-body mappings. *Class. Quant. Grav.*, 35(8):084002, 2018. doi:10.1088/1361-6382/aaa3a8.
- [27] Yeong-Bok Bae, Hyung Mok Lee, Gungwon Kang, and Jakob Hansen. Gravitational radiation driven capture in unequal mass black hole encounters. *Phys. Rev. D*, 96(8):084009, 2017. doi:10.1103/PhysRevD.96.084009.
- [28] Y. Bae, H. Lee, and G. Kang. Gravitational Wave Capture in Spinning Black Hole Encounters. *Astrophysical Journal*, 900(2):175, 2020. doi:10.3847/1538-4357/aba82b.
- [29] Yeong-Bok Bae, Young-Hwan Hyun, and Gungwon Kang. Ringdown gravitational waves from close scattering of two black holes, 10 2023. Preprint arXiv:2310.18686.
- [30] Marc Favata. The Gravitational-wave memory from eccentric binaries. *Phys. Rev. D*, 84:124013, 2011. doi:10.1103/PhysRevD.84.124013.
- [31] K. S. Thorne. Gravitational-wave bursts with memory: The christodoulou effect. *Phys. Rev. D*, 45:520–524, Jan 1992. doi:10.1103/PhysRevD.45.520. URL <https://link.aps.org/doi/10.1103/PhysRevD.45.520>.
- [32] B. Kocsis, M. E. Gaspar, and S. Marka. Detection rate estimates of gravity-waves emitted during parabolic encounters of stellar black holes in globular clusters. *Astrophys. J.*, 648:411–429, 2006. doi:10.1086/505641.
- [33] L. Barsotti, L. McCuller, M. Evans, and P. Fritschel. The a+ design curve. *LIGO Document*, 1800042:2018, 2018.
- [34] Gerald D Quinlan and Stuart L Shapiro. Dynamical evolution of dense clusters of compact stars. *The Astrophysical Journal*, 343:725–749, 1989.
- [35] Jiaru Li, Dong Lai, and Laetitia Rodet. Long-term evolution of tightly packed stellar black holes in agn disks: Formation of merging black hole binaries via close encounters. *The Astrophysical Journal*, 934:154, 8 2022. ISSN 0004-637X. doi:10.3847/1538-4357/ac7c0d.
- [36] Elena Codazzo, Matteo Di Giovanni, Jan Harms, Marco Dall’Amico, and Michela Mapelli. Study on the detectability of gravitational radiation from single-binary encounters between black holes in nuclear star clusters: The case of hyperbolic flybys. *Phys. Rev. D*, 107(2):023023, 2023. doi:10.1103/PhysRevD.107.023023.
- [37] C. Cahillane and G. Mansell. Review of the Advanced LIGO Gravitational Wave Observatories Leading to Observing Run Four. *Galaxies*, 10(1):36, 2022. doi:10.3390/galaxies10010036.
- [38] Unofficial sensitivity curves (ASD) for aLIGO, Kagra, Virgo, Voyager, Cosmic Explorer and ET, 2023. URL <https://dcc.ligo.org/LIGO-T1500293-v13/public>.
- [39] Neil J. Cornish and Tyson B. Littenberg. BayesWave: Bayesian Inference for Gravitational Wave Bursts and Instrument Glitches. *Class. Quant. Grav.*, 32(13):135012, 2015. doi:10.1088/0264-9381/32/13/135012.
- [40] Neil J. Cornish, Tyson B. Littenberg, Bence Bécsy, Katerina Chatziioannou, James A. Clark, Sudarshan Ghonge, and Margaret Millhouse. BayesWave analysis pipeline in the era of gravitational wave observations. *Phys. Rev. D*, 103(4):044006, 2021. doi:10.1103/PhysRevD.103.044006.
- [41] C. J. Moore, R. H. Cole, and C. P. L. Berry. Gravitational-wave sensitivity curves. *Class. Quant. Grav.*, 32(1):015014, 2015. doi:10.1088/0264-9381/32/1/015014.
- [42] Joel Bergé, Richard Massey, Quentin Baghi, and Pierre Touboul. Exponential shapelets: basis functions for data analysis of isolated features. *Mon. Not. Roy. Astron. Soc.*, 486(1):544–559, 2019. doi:10.1093/mnras/stz787.
- [43] Jonah B. Kanner, Tyson B. Littenberg, Neil Cornish, Meg Millhouse, Enia Xhakaj, Francesco Salemi, Marco Drago, Gabriele Vedovato, and Sergey Klimenko. Leveraging waveform complexity for confident detection of gravitational waves. *Physical Review D*, 93(2):022002, January 2016. doi:10.1103/PhysRevD.93.022002.
- [44] M. Drago et al. Coherent WaveBurst, a pipeline for unmodeled gravitational-wave data analysis. *SoftwareX*, 14:100678, 2021. ISSN 2352-7110. doi: <https://doi.org/10.1016/j.softx.2021.100678>.
- [45] Sudarshan Ghonge, Katerina Chatziioannou, James A. Clark, Tyson Littenberg, Margaret Millhouse, Laura Cadonati, and Neil Cornish. Reconstructing gravitational wave signals from binary black hole mergers with minimal assumptions. *Phys. Rev. D*, 102(6):064056, 2020. doi:10.1103/PhysRevD.102.064056.
- [46] M. Millhouse, N. Cornish, and T. Littenberg. Bayesian reconstruction of gravitational wave bursts using chirplets. *Phys. Rev. D*, 97(10):104057, 2018. doi:10.1103/PhysRevD.97.104057.
- [47] C. M. Biwer, C. D. Capano, S. De, M. Cabero, D. A. Brown, A. H. Nitz, and V. Raymond. PyCBC Inference: A Python-based parameter estimation toolkit for compact binary coalescence signals. *Publ. Astron. Soc. Pac.*, 131(996):024503, 2019. doi:10.1088/1538-3873/aaef0b.
- [48] J. Veitch, V. Raymond, B. Farr, W. Farr, P. Graff, S. Vitale, B. Aylott, K. Blackburn, N. Christensen, M. Coughlin, W. Del Pozzo, F. Feroz, J. Gair, C.-J. Haster, V. Kalogera, T. Littenberg, I. Mandel, R. O’Shaughnessy, M. Pitkin, C. Rodriguez, C. Röver, T. Sidery, R. Smith, M. Van Der Sluys, A. Vecchio, W. Vousden, and L. Wade. Parameter estimation for compact binaries with ground-based gravitational-wave observations using the lalinference software library. *Phys. Rev. D*, 91:042003, Feb 2015. doi:10.1103/PhysRevD.91.042003. URL <https://link.aps>.

- org/doi/10.1103/PhysRevD.91.042003.
- [49] K. Cannon, S. Caudill, C. Chan, B. Cousins, J. D. E. Creighton, B. Ewing, H. Fong, P. Godwin, C. Hanna, S. Hooper, R. Huxford, R. Magee, D. Meacher, C. Messick, S. Morisaki, D. Mukherjee, H. Ohta, A. Pace, S. Privitera, I. de Ruiter, S. Sachdev, L. Singer, D. Singh, R. Tapia, L. Tsukada, D. Tsuna, T. Tsutsui, K. Ueno, A. Viets, L. Wade, and M. Wade. GstLAL: A software framework for gravitational wave discovery. *SoftwareX*, 14:100680, June 2021. doi:10.1016/j.softx.2021.100680.
 - [50] B. P. Abbott et al. GWTC-1: A Gravitational-Wave Transient Catalog of Compact Binary Mergers Observed by LIGO and Virgo during the First and Second Observing Runs. *Phys. Rev. X*, 9(3):031040, 2019. doi:10.1103/PhysRevX.9.031040.
 - [51] R. Abbott et al. GWTC-2: Compact Binary Coalescences Observed by LIGO and Virgo During the First Half of the Third Observing Run. *Phys. Rev. X*, 11:021053, 2021. doi:10.1103/PhysRevX.11.021053.
 - [52] R. Abbott et al. GWTC-2.1: Deep Extended Catalog of Compact Binary Coalescences Observed by LIGO and Virgo During the First Half of the Third Observing Run, 8 2021. Preprint arXiv:2108.01045.
 - [53] R. Abbott et al. GWTC-3: Compact Binary Coalescences Observed by LIGO and Virgo during the Second Part of the Third Observing Run. *Phys. Rev. X*, 13(4):041039, 2023. doi:10.1103/PhysRevX.13.041039.
 - [54] B. P. Abbott et al. Tests of General Relativity with the Binary Black Hole Signals from the LIGO-Virgo Catalog GWTC-1. *Phys. Rev. D*, 100(10):104036, 2019. doi:10.1103/PhysRevD.100.104036.
 - [55] R. Abbott et al. Tests of general relativity with binary black holes from the second LIGO-Virgo gravitational-wave transient catalog. *Phys. Rev. D*, 103(12):122002, 2021. doi:10.1103/PhysRevD.103.122002.
 - [56] C. Pankow, K. Chatziioannou, E. A. Chase, T. B. Littenberg, M. Evans, J. McIver, N. J. Cornish, C. Haster, J. Kanner, V. Raymond, S. Vitale, and A. Zimmerman. Mitigation of the instrumental noise transient in gravitational-wave data surrounding gw170817. *Phys. Rev. D*, 98:084016, Oct 2018. doi:10.1103/PhysRevD.98.084016. URL <https://link.aps.org/doi/10.1103/PhysRevD.98.084016>.
 - [57] K. Chatziioannou, N. Cornish, M. Wijngaarden, and T. B. Littenberg. Modeling compact binary signals and instrumental glitches in gravitational wave data. *Phys. Rev. D*, 103(4):044013, 2021. doi:10.1103/PhysRevD.103.044013.
 - [58] S. Ghonge, J. Brandt, J. M. Sullivan, M. Millhouse, K. Chatziioannou, J. A. Clark, T. Littenberg, N. Cornish, S. Hourihane, and L. Cadonati. Characterizing the efficacy of methods to subtract terrestrial transient noise near gravitational wave events and the effects on parameter estimation, 11 2023. Preprint arXiv:2311.09159.
 - [59] Eric Chassande-Mottin, Miriam Miele, Satya Mohapatra, and Laura Cadonati. Detection of gravitational-wave bursts with chirplet-like template families. *Class. Quant. Grav.*, 27:194017, 2010. doi:10.1088/0264-9381/27/19/194017.
 - [60] B. B csy, P. Raffai, N. J. Cornish, R. Essick, J. Kanner, E. Katsavounidis, T. B. Littenberg, M. Millhouse, and S. Vitale. Parameter Estimation for Gravitational-wave Bursts with the BayesWave Pipeline. *Astrophysical Journal*, 839(1):15, April 2017. doi:10.3847/1538-4357/aa63ef.
 - [61] F. Pannarale, R. Macas, and P. J. Sutton. Bayesian inference analysis of unmodelled gravitational-wave transients. *Classical and Quantum Gravity*, 36(3):035011, February 2019. doi:10.1088/1361-6382/aaf76d.
 - [62] B. B csy, P. Raffai, K. Gill, Tyson B. Littenberg, M. Millhouse, and M. J. Szczepa ńczyk. Interpreting gravitational-wave burst detections: constraining source properties without astrophysical models. *Classical and Quantum Gravity*, 37(10):105011, May 2020. doi:10.1088/1361-6382/ab7ee2.
 - [63] C. Henshaw, M. Arogeti, A. Heranval, and L. Cadonati. Visualization of frequency structures in gravitational wave signals. *arXiv e-prints*, art. arXiv:2402.16533, February 2024. doi:10.48550/arXiv.2402.16533.
 - [64] Quentin Baghi, Natalia Korsakova, Jacob Slutsky, Eleonora Castelli, Nikolaos Karnesis, and Jean-Baptiste Bayle. Detection and characterization of instrumental transients in LISA Pathfinder and their projection to LISA. *Phys. Rev. D*, 105(4):042002, 2022. doi:10.1103/PhysRevD.105.042002.
 - [65] A. Refregier. Shapelets: I. a method for image analysis. *Mon. Not. Roy. Astron. Soc.*, 338:35, 2003. doi:10.1046/j.1365-8711.2003.05901.x.
 - [66] A. Refregier and D. Bacon. Shapelets. 2. A method for weak lensing measurements. *Mon. Not. Roy. Astron. Soc.*, 338:48, 2003. doi:10.1046/j.1365-8711.2003.05902.x.
 - [67] Simon Birrer, Adam Amara, and Alexandre Refregier. Gravitational Lens Modeling with Basis Sets. *Astrophysical Journal*, 813(2):102, November 2015. doi:10.1088/0004-637X/813/2/102.
 - [68] Henk Hoekstra, Yanqin Wu, and Andrzej Udalski. An Algorithm to Detect Blends with Eclipsing Binaries in Planet Transit Searches. *Astrophysical Journal*, 626(2):1070–1078, June 2005. doi:10.1086/430299.
 - [69] Adam Amara and Sascha P. Quanz. PYNPOINT: an image processing package for finding exoplanets. *MNRAS*, 427(2):948–955, December 2012. doi:10.1111/j.1365-2966.2012.21918.x.
 - [70] J. A. Ellis and N. J. Cornish. Transdimensional Bayesian approach to pulsar timing noise analysis. *Physical Review D*, 93(8):084048, April 2016. doi:10.1103/PhysRevD.93.084048.
 - [71] G. Desvignes, R. N. Caballero, L. Lentati, J. P. W. Verbiest, D. J. Champion, B. W. Stappers, G. H. Janssen, P. Lazarus, S. Os owski, S. Babak, C. G. Bassa, P. Brem, M. Burgay, I. Cognard, J. R. Gair, E. Graikou, L. Guillemot, J. W. T. Hessels, A. Jessner, C. Jordan, R. Karuppusamy, M. Kramer, A. Lassus, K. Lazaridis, K. J. Lee, K. Liu, A. G. Lyne, J. McKee, C. M. F. Mingarelli, D. Perrodin, A. Petiteau, A. Possenti, M. B. Purver, P. A. Rosado, S. Sanidas, A. Sesana, G. Shaifullah, R. Smits, S. R. Taylor, G. Theureau, C. Tiburzi, R. van Haasteren, and A. Vecchio. High-precision timing of 42 millisecond pulsars with the European Pulsar Timing Array. *MNRAS*, 458(3):3341–3380, May 2016. doi:10.1093/mnras/stw483.
 - [72] Richard Massey and Alexandre Refregier. Polar shapelets. *MNRAS*, 363(1):197–210, October 2005. doi:10.1111/j.1365-2966.2005.09453.x.
 - [73] J. Abadie et al. All-sky search for gravitational-wave bursts in the second joint LIGO-virgo run. *Physical Review D*, 85(12), June 2012. ISSN 1550-2368. doi:10.1103/physrevd.85.122007. URL <http://dx.doi.org/10.1103/physrevd.85.122007>.

- 10.1103/PhysRevD.85.122007.
- [74] B. P. Abbott et al. Observation of gravitational waves from a binary black hole merger. *Phys. Rev. Lett.*, 116:061102, Feb 2016. doi: 10.1103/PhysRevLett.116.061102. URL <https://link.aps.org/doi/10.1103/PhysRevLett.116.061102>.
 - [75] C. Torrence and G. P. Compo. A practical guide to wavelet analysis. *Bulletin of the American Meteorological Society*, 79(1):61–78, 1998.
 - [76] S. Mallat. *A Wavelet Tour of Signal Processing*. Academic Press, 1999.
 - [77] R. M. O’Leary, B. Kocsis, and A. Loeb. Gravitational waves from scattering of stellar-mass black holes in galactic nuclei. *Mon. Not. Roy. Astron. Soc.*, 395(4):2127–2146, 2009. doi:10.1111/j.1365-2966.2009.14653.x.